Supplementary Information A: Data Analysis

This section explains the isolation of the signal due to *direct driving* by the near-field of the modulated electron beam in Figs. 3**b-c** from the parasitic background and the indirect driving by the electromagnetic force. Finally, a qualitative analysis and a quantitative analysis are performed.

Differential Measurement

The ESR signals induced by the near-field of the modulated electron beam are close to the thermal noise level of the selected lock-in amplifier bandwidth of 0.53 Hz. Any stray microwave fields (e.g. from the microwave readout system) at approximately ω_0 can generate parasitic background signals. To mitigate these and other background effects, we perform a differential measurement by recording two data sets: one with the electron beam on $f_{\mathrm{tot}}(\omega)$ and a reference set with the beam off $f_{\mathrm{BG}}(\omega)$, under otherwise identical conditions. Even though the modulation leads to a slight broadening of the signals, this broadening affects both the background and the beam signal equally. As a result, the background can still be subtracted from the total signal despite the non-linearity introduced by the modulation. The lock-in amplifier then detects the first harmonic at ω_m, and due to the linearity of the Fourier transform the subtraction can be carried out explicitly.
Fig. 1**a** shows the two measurements, the difference is shown in **b**. This method allows to isolate the effect of the electron beam from the much larger background signal.

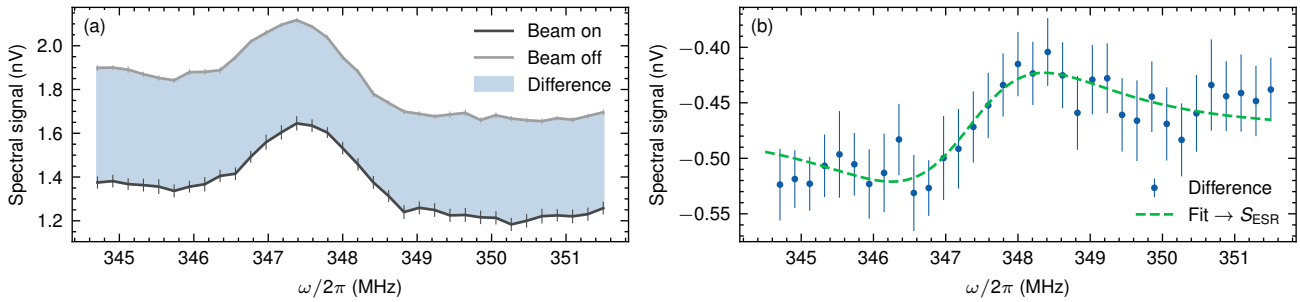

SI Fig. 1. The differential measurement shown in Fig. 3**a** effectively suppresses background contributions and isolates the signal induced by the near-field of the modulated electron beam. We acquire always two datasets, the electron beam switched on **a** and off **b**, yielding the difference in **c** which is fitted using Equ. A3 to extract signal size and phase for data analysis. The offset in **b** is caused by the field modulation, see Section D.

The parasitic ESR signal cannot be attributed to stray fields of our beam modulator, which is operated at the first harmonic $\frac{\omega_0}{2}$. Since our detection setup is only sensitive at the second harmonic ω_0, and the driving signal is low-pass filtered, the fields radiated by the modulator at half the resonance frequency do not contribute to the background signal. It appears that the parasitic ESR signals originate from the local oscillator (LO, see Fig. 4) through an unidentified leakage or coupling mechanism. However, these background contributions are reliably suppressed by the use of differential measurements.

Fitting Procedure

To describe the shape of the ESR spectra, we recall that the solution of the steady-state Bloch equations in the rotating frame gives, with a small driving field with amplitude B_1' at frequency ω and the resonance frequency $\omega_0 = -\gamma_e B_0$, the magnetization components [38]

$$M_{y'} = M_0 \gamma_e B_1' \frac{T_2}{1 + (\omega - \omega_0)^2 T_2^2} \tag{A1}$$

and

$$M_{x'} = M_0 \gamma_e B_1' \frac{(\omega - \omega_0)\, T_2^2}{1 + (\omega - \omega_0)^2 T_2^2}, \tag{A2}$$

where $M_0 = \frac{n_e \gamma_e^2 \hbar^2 S(S+1)}{3 k_B T_s}$ is the thermal magnetization with the spin density $n_e \sim 1.5 \times 10^{27}\,\mathrm{m}^{-3}$ of the BDPA sample, the electron gyromagnetic ratio γ_e, the spin number $S = \frac{1}{2}$ and the sample temperature T_S. Depending on the phase of the LO, a linear combination $M_{y'} \cos(\phi) + M_{x'} \sin(\phi)$ is measured, where $\phi = n\pi,\ n \in \mathbb{Z}$ represents the absorptive case and $\phi = \frac{\pi}{2} + n\pi,\ n \in \mathbb{Z}$ the dispersive case. The lock-in amplifier modulated the resonance frequency ω with $A_m \cos(\omega_m t)$ and thus measures approximately the derivative. We use the fit function (with $k = M_0 \gamma_e B_1'$, $\Delta\omega = \omega - \omega_0$ and an additional offset parameter d)

$$f(\omega, \omega_0, \gamma_2, k, \phi, d) = k \left[\frac{d}{d\omega} \left(\frac{\gamma_2}{\gamma_2^2 + (\Delta\omega)^2} \right) \cos(\phi) + \frac{d}{d\omega} \left(\frac{\Delta\omega}{\gamma_2^2 + (\Delta\omega)^2} \right) \sin(\phi) \right] + d, \tag{A3}$$

where $\gamma_2 = \frac{1}{T_2} = \frac{\sqrt{3}}{2} \Delta\omega_{pp}$ and $\Delta\omega_{pp}$ is the peak-to-peak width of the derivative of the absorptive signal [39].
We extract the signal magnitude from the peak-to-peak voltage of the fitted function $f(\omega, \omega_0, \gamma_2, k, \phi, d)$ (note that variations in γ_2 have an effect on the fitted k value) and use it together with the phase ϕ to determine the two signal quadratures. For the small signals we acquired during the measurements we neglect the variations of ω_0 and γ_2. We attribute variations in the fit parameters ω_0 and γ_2 to the reduced fit quality of the acquired small signals close to the noise floor and therefore neglect them.
Since we employ a lock-in amplification scheme with a modulation amplitude of $B_m \approx 18\,\mu\mathrm{T}$, the peak voltage of the detected signal (which is the first derivative) corresponds only to $\approx 25\,\%$ of the on-resonance signal for absorptive shapes in a hypothetical measurement scenario without a lock-in amplifier.

Magnetic Field Created by the Microcoil Through Beam-Induced Electromotive Force

The modulated beam-induced voltage in the microcoil U_{EMF} causes a current flow limited by the ohmic resistance of the microcoil R_c and the readout system. In the impedance-matched case, the resistance of the readout system is also R_c. Therefore, we approximate the current in the microcoil induced by the modulated beam close to resonance as $\frac{U_{\mathrm{EMF}}}{2R_c}$ (U_{EMF} refers to the voltage in the microcoil, the measured voltage is amplified by the gain of the microcoil impedance match and the readout system). This current creates a magnetic field in x-direction that drives the spins with a $\pi/2$ phase shift relative to B_1^x (sourced by the modulated electron beam), as expected from the time derivative of the law of induction. With $\omega_0 = 2\pi \times 348 \times 10^6\,\mathrm{s}^{-1}$, a coil area $A_{coil} \sim 1 \times 10^{-6}\,\mathrm{m}^2$ and two windings $N_{coil} = 2$ one gets $U_{\mathrm{EMF}} = \mathrm{i} N_{coil} \omega_0 A_{coil} \overline{B_1^x}$. The unitary magnetic field (the field normalized for 1 A current) of our microcoil $B_u \approx 2 \times 10^{-3}\,\mathrm{T\,A}^{-1}$ is varying across the sample for different positions $\vec{r_i}$. Since B_u influences both excitation and detection, we use the self-weighted average $\frac{\sum_i B_u^2(\vec{r_i})}{\sum_i B_u(\vec{r_i})}$. The resulting parasitic driving field is approximated as

$$B_p = I_{coil} B_u = \mathrm{i} \frac{N_{coil} \omega_0 A_{coil}}{2R_c} B_u \overline{B_1^x} \approx \mathrm{i}3 \overline{B_1^x}. \tag{A4}$$

The ratio of the signals can be thus approximated as $S_{\mathrm{EMF}}/S_{\mathrm{beam}} \approx 3\mathrm{i}$ (see the ratio between $S_{\mathrm{ESR}}(d = 0)$ and $S_{\mathrm{ESR}}(d \approx 0.7)$ in Fig. 2**b**). The resulting signal becomes (with $\alpha = R \frac{B_u}{2R_c}$)

$$S_{\mathrm{EMF}} = R \cdot \overline{B_1^x} = \alpha U_{\mathrm{EMF}}, \tag{A5}$$

where $R \approx 4\,\mathrm{V\,T}^{-1}$ is the ratio ESR signal to the driving field that can be determined using conventional ESR measurements (see Fig. 5**d**), involving a coarse estimate of the driving field. This gives a good estimate for S_{EMF} and can be used to recover the direct driving signal S_{beam}.

Phase Alignment

To retrieve the direct driving signal we have to subtract the estimate of the indirect driving signal S_{EMF} from the measured ESR signal. As a prerequisite the phases of the two measurement devices (Lock-in amplifier measuring S_{ESR} and the LTC5584 I-Q-demodulator measuring U_{EMF}, see Fig. 4 for a more detailed schematic) have to be aligned. We achieve this by leveraging the constant offset in the ESR spectrum (see Fig. 1**b**), which is caused by the modulation field B_m (see Section D) of the electron beam. The U_{EMF} signal is mainly in one quadrature (except for spurious signals) and $\propto B_1^x$. By taking two ESR measurements in the U_{EMF} maximum or mininum (see Fig. 9) with a 90° relative phase shift and determining the offsets d_I and d_Q, the phase shift of S_{ESR} relative to U_{EMF} is determined by $\arctan(d_I/d_Q)$.

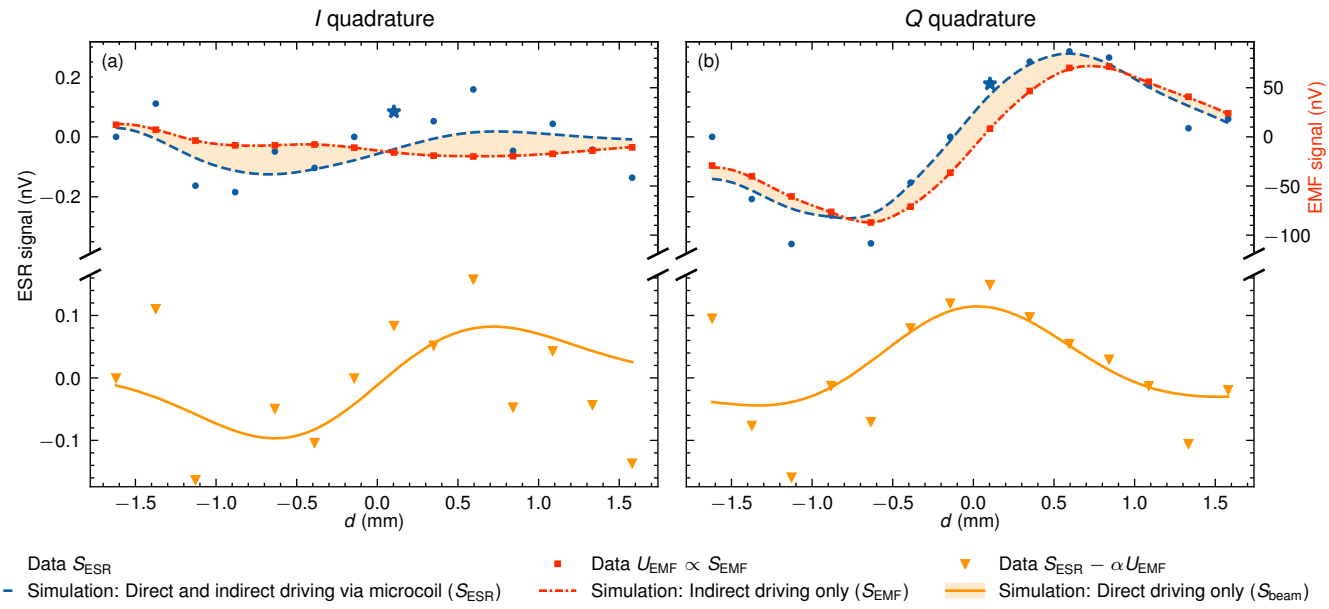

SI Fig. 2. I and Q quadratures of the signals induced by a modulated electron beam at $h \approx 0.45\,\mathrm{mm}$ for different d. The indirect driving signal S_{EMF} was estimated from the measured U_{EMF} and then subtracted from the measured ESR signal S_{ESR} to recover the direct driving signal S_{beam}. For the latter the quadratures correspond to the magnetization components driven by the B_1^x and $-B_1^y$ field amplitudes, respectively. Due to the additional induction, the indirect driving signal is phase shifted by 90°, hence the B_1^x field component induced into the microcoil appears in the Q quadrature, which facilitates the disentanglement of the two effects (one has its maximum close to $d = 0$, the other a zero-crossing).

Qualitative Analysis

Using Equ. A4 and A5 we can recover the signal caused by direct driving of the electron beam's near-field. This can be simplified to a single factor $\alpha = R\frac{B_u}{R_c}$ (R_c is the microcoil resistance, B_u the coupling of the microcoil to the spins in $\mathrm{T\,A^{-1}}$ and R in $\mathrm{V\,T^{-1}}$ the ESR signal to driving field ratio, determined from conventional ESR scans (see Fig. 5**d**) yielding:

$$S_{\mathrm{beam}} = S_{\mathrm{ESR}} - \alpha U_{\mathrm{EMF}}. \tag{A6}$$

The three components of this equation are shown as triangles, dots and squares in Fig. 2 (which shows both signal quadratures for a beam at $h \approx 0.45\,\mathrm{mm}$ for different d, as in Fig. 3**b**). Due to the induction, U_{EMF} exhibits an additional 90° phase shift and thus adds to the B_1^y component of the near-field which exhibits a maximum close to $d = 0$, as opposed to the former with the zero-crossing, which simplifies the separation of direct and indirect driving fields (in the Q quadrature). The I quadrature comprises the B_1^x component of the direct driving and residual induction into the microcoil. It should be noted that due to the uncertainy in the phase alignment (see above) the direct and indirect effect of the B_1^x field component can mix between the two quadratures.
These results demonstrate that the direct driving signal can be recovered using a single scaling factor, leading to a clear observable shift of the measured ESR signal S_{ESR} along d with respect to the measured electromotive force in the microcoil (U_{EMF}).

Quantitative Analysis Using Simulations

In addition to the qualitative analysis performed above, the ESR measurements have been analyzed quantitatively to approximately validate the signal size (limited by uncertainties in the gain factors of the microcoil impedance match, the readout system and inaccuracies of the conventional ESR data). The solid lines in Fig. 2 show the simulations, which are described in Section E. A sample size of $1.1 \times 0.7 \times 0.7\,\mathrm{mm}^3$ was assumed and an estimate of the sample density was determined by conventional ESR measurement. The sample density and coil resistance were then adjusted

for the simulations to fit the measured data, yielding $\approx 0.5 n_e$ and $\approx 1.25\,\Omega$, respectively. These are reasonable values, since the former varies between BDPA samples [40] and the latter was estimated to $\approx 1.75\,\Omega$ using the impedance match and $\approx 0.6\,\Omega$ from conventional ESR saturation scans. The data agree with the simulation, though the deviations are larger than those for the I quadrature. This can be explained by the fact that the total signal S_{ESR} is larger prior to subtraction. Since spline interpolated U_{EMF} data have been used for simulation of S_{EMF}, this explains the non-zero S_{EMF} in Fig. 2**b**.

Analysis Summary

We observe three signals which are different in size: (1) the parasitic ESR signal, which is subtracted by performing differential measurements, (2) S_{EMF} the indirect driving with the electron beam via the microcoil, and finally (3) S_{beam} the direct driving of spins by the near-field of the modulated electron beam. The last two can be disentangled because (2) experiences a 90° phase shift during the induction. The sum (2)+(3) exhibits a zero-crossing being shifted along d with respect to the electromotive force induced in the microcoil. Finally, quantitative analysis has been used to confirm the measured signals.

Supplementary Information B: Experimental Setup

Scanning electron microscope: We utilize a Philips XL30 scanning electron microscope (SEM), equipped with a thermionic tungsten filament electron source, as our experimental platform. Two condenser lenses and various apertures collimate the beam.

Since our experiment requires a sufficiently large magnetic near-field of the modulated electron beam we tried to maximize the beam current of the SEM while keeping basic imaging capabilities. We selected a 600 µm final aperture and achieved currents in the range of ∼2.5-5.5 µA at 10 keV ($v_e \approx 0.2c$) in the sample region. We accomplished this by adjusting the position of the filament within the Wehnelt-cylinder and adjusting the bias voltages to project a larger portion of the filament tip towards the sample.

The non-standard operation regime yields unstable emissions. We attribute these to thermally induced filament deformation and deterioration that manifests both on a timescale of minutes, after enabling the beam and on a multiple hours timescale via slow drifts. In addition, the beam current exhibits a position dependence. To compensate for those systematic errors, we measured the beam current via a copper foil on the bottom of the SEM chamber and rescaled our measurements accordingly.

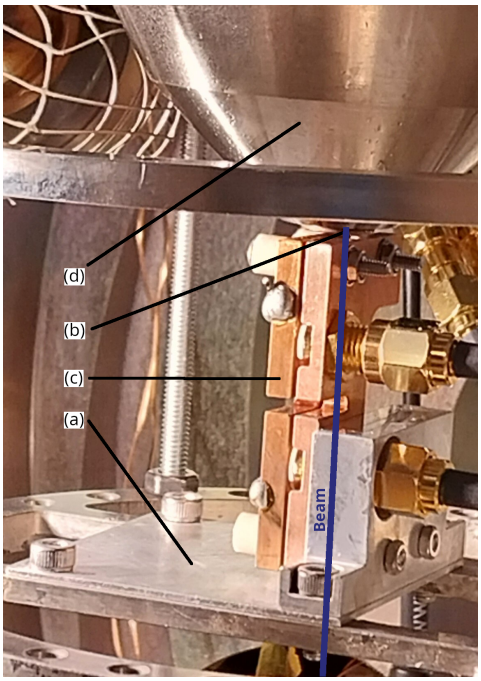

SI Fig. 3. The 4 mm diameter 40 mm long custom deflection plates **c** are mounted on the SEMs pole shoe **d** in front of the final lens assembly and final aperture **b**. The aluminum plate **a** prevents beam distortions below the deflection plates.

Beam Modulation: For spatial electron beam modulation, we built a custom beam modulator (see Fig. 3**c**) which consists of two half-cylindrical (radius 2 mm) copper plates, each 40 mm long, spaced 500 µm apart. The modulator is mounted on a cage system that is fixed in front of the pole piece. A grounded aluminum plate (depicted in Fig. 3**a**) shields against stray fields of the modulator assembly to further prevent deflection of the electron beam after it has passed the modulator. One of the deflection plates remains at ground potential and attaches directly to the pole piece, while the other one connects to a coaxial cable that delivers a microwave signal at half the readout frequency ω, which is $\frac{\omega}{2} \approx 2\pi \times 175$ MHz. The microwave signal is then routed outside the SEM and terminated with a 50 Ω resistor to avoid thermal load inside the vacuum chamber of the microscope (see Fig. 4). Since the beam modulation occurs at around half the resonance frequency ω_0, additional shielding to suppress direct microwave driving of the sample is not required. This beam modulator allows for deflection amplitudes of up to 2 mm at the sample position 130 mm below the pole piece.

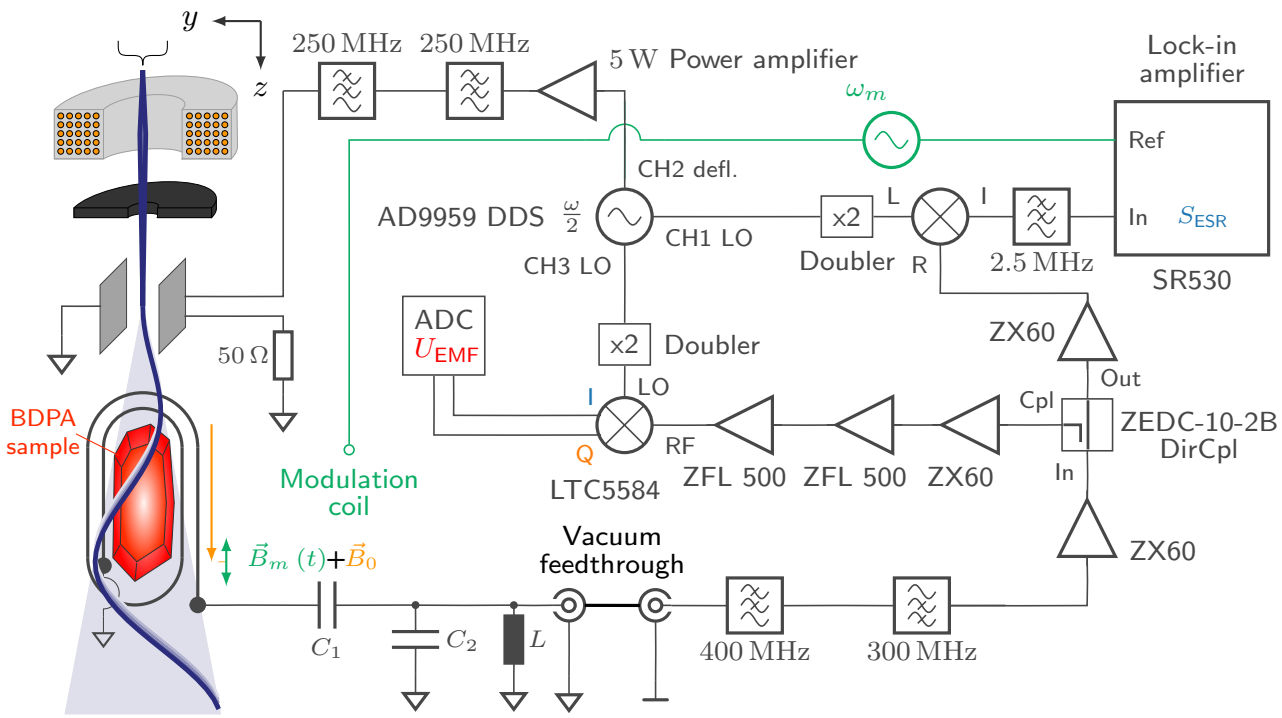

SI Fig. 4. To measure the electromotive force (EMF) signal originating from the modulated electron beam induced spin precession, we use a lock-in detection scheme. The signal is inductively coupled to an impedance matched microcoil subsequently filtered and amplified. A directional coupler (DirCpl) splits it into: **CPL port** to directly monitor the near-field of the modulated electron beam and **Out port** for lock-in ESR measurements. In the excitation chain (CH2 defl), we utilize filters to prevent 2nd order and higher harmonics leaking from the beam modulator and thus parasitically driving the sample via radiated fields. The local oscillators (CH1 and CH3 of our DDS) are frequency doubled since our DDS only supports frequencies up to 250 MHz.

Sample stage: The miniaturized ESR-setup is mounted on a custom stage, attached to a port aligner, in order to adjust the position of the ESR-sample relative to the electron beam.

Microwave setup: The microwave setup is depicted in Fig. 4. The spin precession of our sample is inductively sensed by the microcoil (see Fig. 5**b**). This coil is impedance-matched to 50 Ω at ≈ 350 MHz using an L-type capacitive matching network ($C_1 = 47\,\text{pF}, C_2 = 18\,\text{pF}$). A small inductance of $L = 390\,\text{nH}$ in parallel is used to protect our microwave electronics against low frequency high voltages. Subsequently, a low-pass (400 MHz) and high-pass (300 MHz) filter select the 2$^{\text{nd}}$ harmonic components. This step mitigates microwave background saturating the amplifiers. The filtered signal is amplified via one ZX60-P103LN+ low-noise amplifier. The signal is then split using a ZEDC-10-2B directional coupler in two paths: The **Out** port is amplified with a ZX60 low-noise amplifier. The signal is then extracted employing microwave down-mixing with a local oscillator (L) and low-pass filtered at 2.5 MHz, to discard high-frequency sidebands. Subsequently a SRS-SR530 lock-in amplifier records the signal S_{ESR}. The **Cpl** port is amplified (1x ZX-60, 2x ZFL-500LN+) and used to monitor the two quadratures I and Q (see Fig. 1**b**) of the signal U_{EMF} induced by the electron beam via an LTC5584 I/Q demodulator, whose outputs are processed by two ADC channels of an RP2040 microcontroller. The latter signal is also used to estimate the electron beam position.

The microwave signal used to deflect the electron beam is sourced by a AD9959-based Direct Digital Synthesizer (DDS) (CH2, see Fig. 4) amplified by a 5 W power amplifier and subsequently low pass filtered to suppress higher harmonics, thus preventing parasitic sample excitation by leaking fields. Since the DDS supports frequencies only up to 250 MHz, CH1 and CH3 are passively frequency-doubled (FD-2+) and high pass filtered (> 300 MHz), and used as local oscillators (LO) in the I/Q-demodulator as well as the ESR mixer chain.

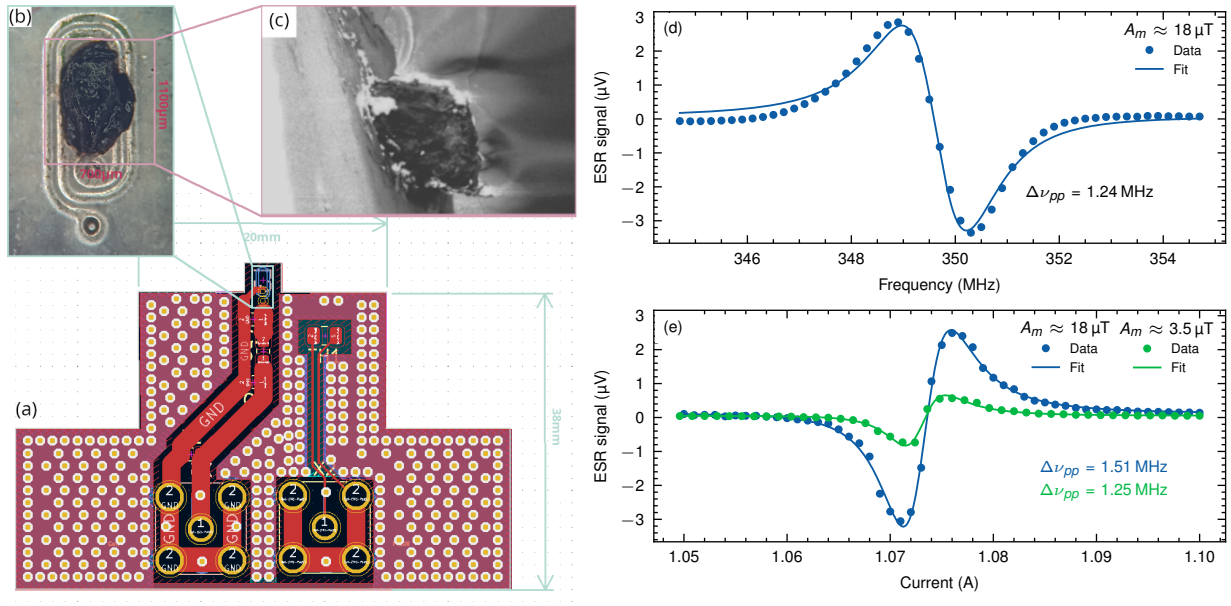

SI Fig. 5. **a** Detailed view of the PCB layout in the design software. The vias spread over the surface are used for thermal management and contact to our stage ground. **b** Top view of the PCB with a BDPA sample (which was used in another measurement) inside the microcoil. **c** SEM image of the sample. The curved lines to the top of the sample are caused by charging effects on the non conductive surface of the sample and due to the fact that the beam is blocked on a wrinkled conductive foil used as Faraday cup 35 mm below the sample. The geometry appears slightly curved due to the extension of the PCB and sample along the beam-axis as well as the applied B_0 field which causes a position dependent twist of the image plane. **d**, **e** show conventional ESR spectra employing a directional coupler to excite and sense the sample via the microcoil by performing **d** a frequency sweep and **e** a current sweep. The modulation amplitude applied during the measurements involving the electron beam ($A_m \approx 18\,\mu T$) causes a slight broadening (**e**). The fitted signal in **d** shows a narrow absorption linewidth, which may be attributed to the frequency dependence of the microwave setup.

Supplementary Information C: Microcoil and Sample Preparation

The microcoil sensing for ESR signals is fabricated on a printed circuit board (PCB, depicted in Fig. 5**a**). The PCB uses a standard 1.6 mm FR-4 core with 35 µm copper layers on both sides. The microcoil (see Fig. 5**b**) is printed on the opposite side of the matching network (see Fig. 5**a**). This design prevents the electron beam hitting the matching network and creating parasitic signals and noise in the readout circuit.

For the spin ensemble in our experiment, we used a BDPA crystal $1.1 \times 0.7 \times 0.7\,mm^3$, which is placed atop a groove within the microcoil and fixed with small amounts of vacuum grease (see Fig. 5**b**). The single crystal extends ∼700 µm above the PCB surface.

We estimated the microcoil resistance R_c to be on the order of $1\,\Omega$ at $\omega_0 \approx 2\pi \times 350\,MHz$.

All copper layers are grounded to discharge unwanted surface charges deposited by the electron beam. To further reduce beam distortion by charging effects, the surface of the PCB including the microcoil was coated with a ∼10 nm thick 60:40 gold-palladium layer on top of an insulating solder mask.

To evaluate the Q-factor of the combined coil and impedance matching setup, we measured the resonance depth and bandwidth. At 350 MHz the Q-factor was determined to be approximately 100 with a resonance depth of 22 dB and a bandwidth of 3 MHz.

We first characterized the sample and measurement setup by performing conventional ESR measurements, by exciting the sample directly with the microcoil with a driving field injected via a directional coupler (DirCpl) inserted directly at the vacuum feedthrough (the driving field then amounts to a few µT, i.e. below saturation which would occur at ∼ 100 µT for BDPA) and measuring the spin precession at the coupling port of the DirCpl. A spectrum recorded this way, with a frequency sweep, is shown in Fig. 5**d** for a modulation amplitude $A_m \approx 18\,\mu T$. Fig. 5**e** depicts the same spectrum with a B_0 sweep at constant frequency $\omega_0 = 2\pi \times 349.7\,MHz$. The smaller linewidth in the frequency sweep (at $A_m \approx 18\,\mu T$) is most likely explained by the convolution with the narrow impedance match of the microcoil. Lock-in detection with a modulated B_m-field broadens the linewidth from $\Delta\omega_{pp} \approx 2\pi \times 1.25\,MHz$ at low A_m to $\approx 2\pi \times 1.5\,MHz$ for $B_m = 18\,\mu T$ (see Fig. 5**e**). From the current sweep at low $A_m \approx 3.5\,\mu T$ we determined

a transversal relaxation time $T_2 \approx 147\,\mathrm{ns}$, consistent with previously reported values [40, 41].

Supplementary Information D: Phase Calibration

The modulated electron beam also causes an additional background in the ESR spectrum, shown in Fig. 6**a** - the I and Q data were taken with two measurements with a 90° phase shift of the LO. The modulation for the lock-in detection also shifts the beam position due to the Lorentz force inducing an EMF at the lock-in modulation frequency in the microcoil, which can be detected by the lock-in amplifier. This is expected to give a constant offset in the signal, limited by the impedance match of the microcoil. However, since we perform frequency sweeps, different microwave path lengths from the frequency source (DDS) to the R port and the L port of the mixer (see Fig. 4) cause the signal to move between the quadratures, explaining the observed behavior. To fit this behavior, we use a function g, which is a combination of a cosine and the impedance match

$$g(\omega, k, a, \theta, \omega_0, s) = k\cos(a\omega + \theta) \cdot \frac{1}{\sqrt{\left(\frac{\omega-\omega_0}{s}\right)^2 + 1}}, \tag{D1}$$

where $k\cos(a\omega + \theta)$ describes the frequency-dependent shift of the signal in and out the quadrature with factor a (unit is s) for the frequency ω, to get the "frequency" of the phase shift and a phase ϕ, and $\frac{1}{\sqrt{(\omega-\omega_0)^2/s^2+1}}$ fits the impedance match of the coil with resonance frequency ω_0 and width s. In Fig. 6**b**, magnitude and phase are plotted. By adding a frequency dependent phase to the LO, one can compensate for the phase shift, yielding a nearly flat background, only affected by the frequency dependence of our microwave setup (see Fig. 1**b**). Fig. 6**c**, **d** show the frequency dependence of the EMF of the electron beam.

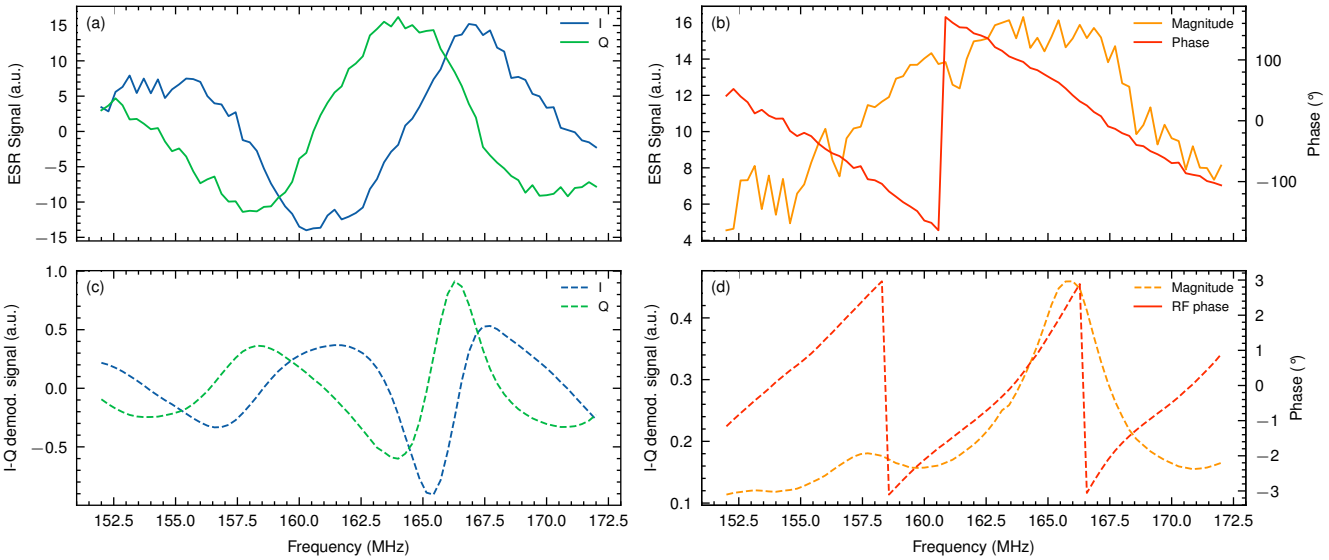

SI Fig. 6. Due to different cable lengths and other phase shifting elements in our setup, the phase relation between the exciting microwave input and reference LO input at our mixer (or I-Q-demodulator in case of the electron beam-induce EMF) changes with frequency ω. **a**, **b** for our ESR scans, we only measure one quadrature at a time. I and Q refer to two different measurements with 90° phase difference. The signal in **a** is a residual electron beam EMF caused by the modulation coil, which slightly affects the beam. We use the linear phase dependence in **b** to shift the LO, thereby removing the frequency dependence and always maintain the same relative phase. A signal offset (which still varies with the LO phase) remains (see Fig. 1**b**). **c**, **d** In case of the electron beam EMF, both quadratures are recorded simultaneously and can be used to determine magnitude and phase. The impedance match of the microcoil can be seen in the EMF magnitude (note that the measurements in this figure were taken with a different PCB).

Supplementary Information E: Finite-Element Simulation

To model the ESR signals, a finite element simulation of the sample was carried out for the magnetic near-field B of the modulated electron beam driving the sample. We assume a cuboid sample geometry of $1.1 \times 0.7 \times 0.7\,\mathrm{mm}^3$, inferred from microscopic images (see Fig. 5**b**). The spin density was first estimated to $\approx 0.25 n_e$, using the signal amplitude observed in the conventional ESR measurement shown in Fig. 5**d** and later adjusted to $\approx 0.5 n_e$ to match the data involving the electron beam. This deviation is acceptable when considering errors in gain of the impedance match, the setup inside the vacuum chamber, of our readout setup and the fact that the driving fields in conventional ESR are not precisely known.

The simulation was performed on a rectangular grid composed of voxels with a side length of 100 µm. The results reveal a pronounced spatial dependence of the driving field, arising from the near-field of the electron beam and its position relative to the sample (shown as solid lines in Fig. 3**b**, and as orange solid lines in Figs. 2 and 10).

Simulation of the near-field

The electron beam is modeled as an infinitely long thin beam at position $(x, y) = (h, d)$ that is moving side-by-side of the observer with frequency $\omega/2$ at position $\mathbf{r} = \big(x, y, 0\big)$. Using Ampère's law the time dependent magnetic field becomes (using [31], Eq. G3)

$$\mathbf{B}\left(\mathbf{r}, t\right) = -\frac{\mu_0 I}{2\pi} \frac{\begin{pmatrix} y - d - A\cos\left(\frac{\omega}{2}t\right) \\ h - x \\ 0 \end{pmatrix}}{\left(y - d - A\cos\left(\frac{\omega}{2}t\right)\right)^2 + \left(h - x\right)^2}. \tag{E1}$$

The harmonic components are then determined numerically by calculating the field for different t and performing a Fourier transform. Fig. 7 shows the beam modulation (sketched only in the xy plane) relative to the sample. The 5° angle of the deflection direction with respect to the y-axis is also considered in the simulations, leading to a slight modification of Eq. E1. In addition, finite element simulations have been conducted using Biot Savart's law, showing that the approximation of the beam as infinite line agrees unless $A \gg h$, which is sufficient for this experiment.

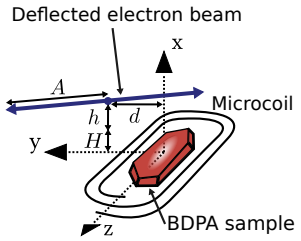

SI Fig. 7. Sketch of the electron beam deflection in the xy plane (only 2D representation) with respect to the spin sample and the microcoil, including the tilt and the beam position d and h (the origin is in the center of the microcoil, h is the distance from the top of the sample with height $H = 0.7\,\mathrm{mm}$.

Bloch Equations

The near-field of the modulated electron beam exhibits two field components, hence the Bloch equations ([38], Eqs. 10.14 and 10.17; T_1 and T_2 are the longitudinal and transverse relaxation times, respectively)

$$\frac{\mathrm{d}\mathbf{M}}{\mathrm{d}t} = \gamma_e \mathbf{M} \times \widetilde{\mathbf{B}} - \frac{1}{T_1}\begin{pmatrix} 0 \\ 0 \\ M_z - M_0 \end{pmatrix} - \frac{1}{T_2}\begin{pmatrix} M_x \\ M_y \\ 0 \end{pmatrix} \tag{E2}$$

have to be solved for two driving field components with amplitudes B_1^x and B_1^y and phases θ_x and θ_y to be included in the simulations. For

$$\widetilde{\mathbf{B}} = \begin{pmatrix} B_1^x \cos(\omega t + \theta_x) \\ B_1^y \cos(\omega t + \theta_y) \\ B_0 \end{pmatrix} \tag{E3}$$

we can transform the equations into the rotating frame using

$$R_z\left(-\omega t\right) = \begin{pmatrix} \cos\left(\omega t\right) & -\sin\left(\omega t\right) & 0 \\ \sin\left(\omega t\right) & \cos\left(\omega t\right) & 0 \\ 0 & 0 & 1 \end{pmatrix}. \tag{E4}$$

Solving the equations for low driving powers leads to the magnetization components

$$M_{x'} = -\frac{M_0 \gamma_e T_2}{1 + (\Delta\omega T_2)^2} \left(B_1^{y'} - T_2 \Delta\omega B_1^{x'} \right) \tag{E5}$$

and

$$M_{y'} = \frac{M_0 \gamma_e T_2}{1 + (\Delta\omega T_2)^2} \left(B_1^{x'} + T_2 \Delta\omega B_1^{y'} \right), \tag{E6}$$

where $B_1^{x'} = \frac{1}{2} \left(B_1^x \cos\theta_x - B_1^y \sin\theta_y \right)$ and $B_1^{y'} = \frac{1}{2} \left(B_1^x \sin\theta_x + B_1^y \cos\theta_y \right)$.
Transforming back from the rotating frame (using $R_z(\omega t)$ the magnetization components become

$$\begin{aligned} M_x &= \mathrm{Re}\left[\left(M_{x'} - \mathrm{i} M_{y'} \right) e^{\mathrm{i}\omega t} \right] \\ M_y &= \mathrm{Re}\left[\mathrm{i} \left(M_{x'} - \mathrm{i} M_{y'} \right) e^{\mathrm{i}\omega t} \right]. \end{aligned} \tag{E7}$$

The spin-induced EMF signal can then be calculated using the principle of reciprocity [42]. We define $\mathbf{B}_u = (B_u^x, B_u^y, B_u^z)$ as the magnetic field at the position of the sample that is generated by a 1 A current through the microcoil with units T/A. Then, equation (2) of [42] implies for the voltage that is induced in the microcoil due to the magnetization of the sample (with the voxel volume V_v, Arg denotes the argument of a complex number)

$$U = -V_v \frac{d}{dt} \mathbf{B}_u \cdot \mathbf{M} = \mathrm{Re}\left[i\omega V_v \left(B_u^x + \mathrm{i} B_u^y \right) \left(M_{x'} - \mathrm{i} M_{y'} \right) e^{i\omega t} \right] = 2\mathrm{Re}\left[U_0 e^{i\omega t} \right] = |U_0| \cos\left(\omega t + \mathrm{Arg}\, U_0 \right) \tag{E8}$$

with

$$U_0 = \frac{\mathrm{i}}{2} \omega V_v \left(B_u^x + \mathrm{i} B_u^y \right) \left(M_{x'} - \mathrm{i} M_{y'} \right) \propto B_1^x e^{\mathrm{i}\theta_x} - \mathrm{i} B_1^y e^{\mathrm{i}\theta_y}. \tag{E9}$$

Therefore, magnitude and phase of the signal U depend on the interference of the x and y field components in the rotating frame and we can regard $B_1^x e^{\mathrm{i}\theta_x} - \mathrm{i} B_1^y e^{\mathrm{i}\theta_y}$ as the driving field of the spins. Since $\omega_0 = -\gamma_e B_0$ the spins precess around the negative z axis which explains the minus sign for B_1^y.
In the finite-element simulations, the signal induced into the microcoil is calculated as the sum of the complex U_0 which are calculated for each voxel using Equ. E9.

Indirect Driving

The simulations for data analysis are based on the spline interpolation of the measured U_{EMF} values (see Fig. 9). The corresponding driving field is calculated for every finite element, (see Section E), as

$$B_{\mathrm{EMF}}\left(\vec{r_i}\right) = \left(B_u^x\left(\vec{r_i}\right) + \mathrm{i}B_u^y\left(\vec{r_i}\right)\right)\frac{U_{\mathrm{EMF}}}{2R_c}. \tag{E10}$$

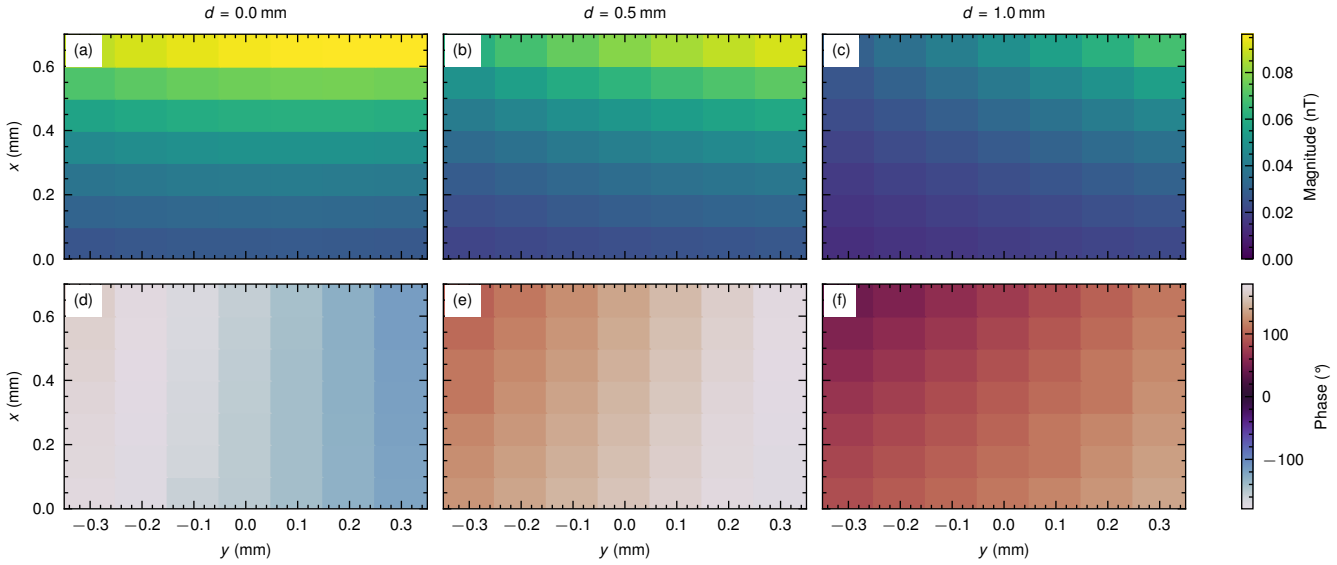

SI Fig. 8. Spatial dependence of the complex magnetic field $B_1^x - \mathrm{i}B_1^y$ of the modulated electron beam at 1 µA, as experienced by the sample (voxels with 100 µm side length), averaged along the z-axis. The origin of the coordinate system is found in the center of the microcoil, see Fig. 7. **a-c** depict the magnetic field magnitudes for different electron beam positions along the y-axis ($h = 0.6$ mm) with a deflection amplitude $A = 0.9$ mm approximately along the y-axis (tilted by 5° into the xy-plane) nearby the sample. **d-f** display the corresponding phases, which also exhibit a significant spatial dependence.

Variation of the driving field across the sample

Fig. 8 shows the simulation of the complex magnetic field $B_1^x - \mathrm{i}B_1^y$ experienced by different voxels at various electron beam positions along the y-axis ($h = 0.6$ mm), averaged along the symmetric z-axis (beam direction).
For the simulation, we assumed a beam deflection with an amplitude of 0.9 mm along the y-axis for several beam positions d at $h = 0.6$ mm under an angle of 5° relative to the y-axis, as sketched in Fig. 7. Fig. 8**a-c** illustrate how the field magnitude at the sample position decreases with distance, while Fig. 8**d-f** shows the spatially varying phase of the driving field.
This spatial dependence could be used in future applications to create painted potentials or to enhance spatial resolution.

Supplementary Information F: Near-Field Induced Electromotive Force

During the ESR measurements, the electromotive force (U_{EMF}) due to the modulated electron beam in the microcoil is simultaneously recorded (see Section B). The differential measurement allows to recover the field of the electron beam $b\cos(\omega t + \phi_2)$ by assuming that we measure the superposition $C\cos(\omega t + \phi) = a\cos(\omega t + \phi_1) + b\cos(\omega t + \phi_2)$ when the electron beam is on and the signal background $a\cos(\omega t + \phi_1)$ when the electron beam is off. In the complex representation we get $Ce^{i\phi} - ae^{i\phi_1} = be^{i\phi_2}$.
The magnetic field amplitude $\overline{B_1^x}$ in x-direction, averaged over the coil area, is calculated from the modulated beam

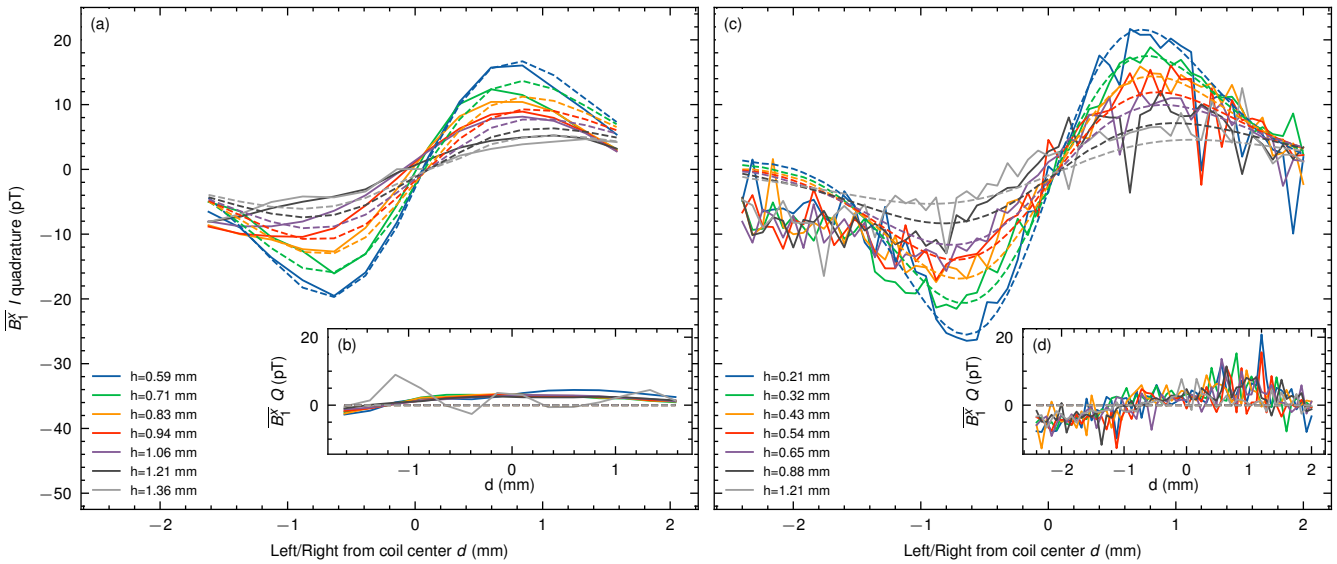

SI Fig. 9. Second harmonic Fourier component of the magnetic near-field of the modulated electron beam in x-direction ($\overline{B_1^x}$) inferred using the electromotive force (EMF) induced in the microcoil normalized to 1 µA beam current. Two quadratures I and Q of the detected signal are shown in **a,c** and **b,d**, respectively. **a**, **b**: The data was recorded at the same time as the data in Fig. 10. With an approximate beam deflection amplitude of 0.9 mm nearby the sample at $\omega = 2\pi \times 174$ MHz we determined scaling and distances comparing it to simulations. The scaling along the x-axis had to be corrected by a factor 0.5. **c**, **d**: Fast data recording at $\omega = 2\pi \times 174$ MHz: No ESR spectra were taken simultaneously. The data are in agreement with the position scaling determined from from SEM images.

induced voltage U_{EMF}, which is extracted from the differential measurement (see Section A), using

$$\overline{B_1^x} = \frac{U_{\mathrm{EMF}}}{\omega N_{\mathrm{coil}} A_{\mathrm{coil}}}, \tag{F1}$$

where A_{coil} is the coil area and N_{coil} the number of coil windings. $\overline{B_1^x}$ is used to determine the position of the microcoil relative to the electron beam (the scaling along the x-axis and y-axis as well as the deflection amplitude have been estimated using the imaging capabilities of the SEM). Fig. 9**c**, **d** show a $\overline{B_1^x}$ measurement at $\omega = 2\pi \times 174$ MHz (∼5 s per position and no ESR spectra recorded). In contrast, the data from the ESR measurements (∼20 min per position) shown in Fig. 9**a**, **b** reveal a slightly different behavior along the x-axis (moving away from the sample), which we attribute to charging and/or drifts of the electron beam position. To account for these, we rescale the x-axis accordingly. The asymmetry between the two peaks in **a** is attributed to the small angle of 5° between the deflection- and y-axis (see Fig. 7).

As predicted by theory, $\overline{B_1^x}$ can be aligned to fit in one quadrature (I, in Fig. 9**a**, **c**). However, some smaller residuals are found in the Q quadrature (Fig. 9**b**, **d**).

Supplementary Information G: Resonance Shift from Electron Beam's DC Component

For a 4 µA beam at a distance of 100 µm from the sample, our numerical simulations estimate the DC component of the magnetic field to be below 10 nT (see Section E). With a resonance frequency of ∼28 GHz T^{-1}, this limits the maximum shift of the ESR resonance frequency to 280 Hz and should therefore, not cause any significant line shift that could resemble the shape of a signal when performing differential measurements.

Supplementary Information H: Detailed Spatial Dependence

Detailed scans for different (h, d) are shown in Fig. 10, exhibiting the signal driven by the two field components B_1^x and B_1^y along d and a decay along h. While the total S_{ESR} and indirect driving signal S_{EMF} depicted in the second

column is clearly visible also for larger distances h the smaller direct driving signal S_{beam} on the third and fourth columns vanishes quickly.

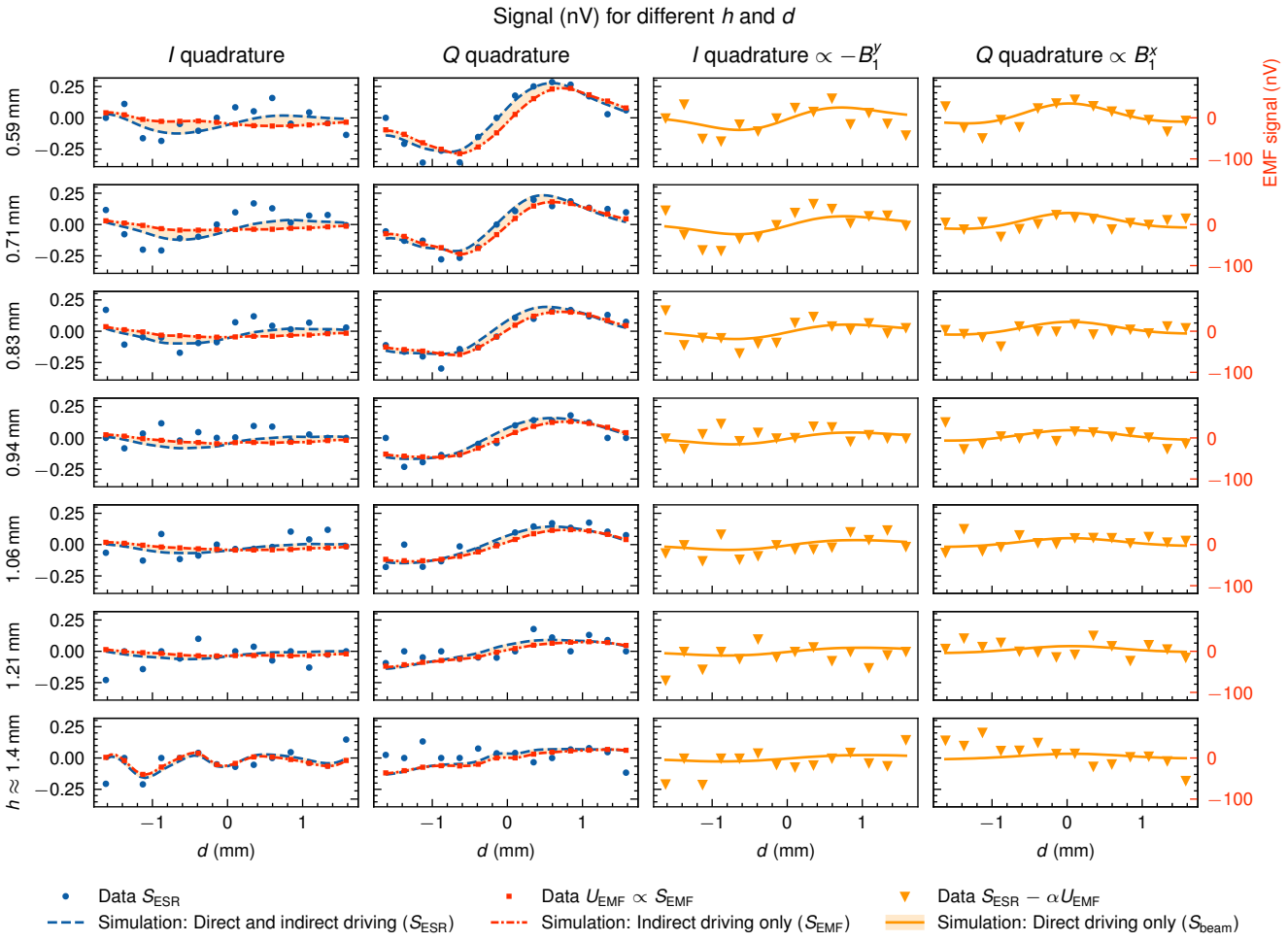

SI Fig. 10. Overview of all fitted data points used in Fig. 3**c**. Each line shows the data for a certain h, the two left columns show the S_{ESR}, U_{EMF} and S_{EMF} signal compared to simulations. The two right columns depict the two quadratures of the recovered S_{beam} signal that is directly driven by the modulated electron beam, again comparing to simulations. The measurement conditions are the same as the measurement shown in Fig. 3**b**, except for the different h.

[38] Weil, J. A. *Electron paramagnetic resonance: elementary theory and practical applications* (Wiley-Interscience, 2007), 2nd edn.

[39] Eaton, G. R., Eaton, S. S., Barr, D. P. & Weber, R. T. *Quantitative EPR* (Springer Vienna, Vienna, 2010).

[40] Mitchell, D. G. *et al.* Electron Spin Relaxation and Heterogeneity of the 1:1 α,γ-Bisdiphenylene-β-phenylallyl (BDPA)/Benzene Complex. *The Journal of Physical Chemistry B* **115**, 7986–7990 (2011).

[41] Goldsborough, J. P., Mandel, M. & Pake, G. E. Influence of exchange interaction on paramagnetic relaxation times. *Phys. Rev. Lett.* **4**, 13–15 (1960).

[42] Hoult, D. & Richards, R. The signal-to-noise ratio of the nuclear magnetic resonance experiment. *Journal of Magnetic Resonance (1969)* **24**, 71–85 (1976).